Supplementary Information for

Reversible Acidification Enables Closed-Loop Total Separation of Olivine

Anatole Borisov[1], Kunal Lodaya[1], Dharik Mallapragada[2], Yogesh Surendranath[1,3*]

[1]Department of Chemistry, Massachusetts Institute of Technology, Cambridge, Massachusetts 02139, United States

[2]Department of Chemical and Biomolecular Engineering, Tandon School of Engineering, New York University

[3]Department of Chemical Engineering, Massachusetts Institute of Technology, Cambridge, Massachusetts 02139, United States

*Corresponding Author: yogi@mit.edu

Table of contents

16

17

Supplementary Notes

1. Discussion on SO_2 Aerobic Oxidation

The 'uncatalyzed' rates of SO_2 oxidation by air in water are very slow, on the order of 10^{-9} M/s. However, even trace Fe and Mn ions can catalyze the reaction, which historically led to challenges in measuring the 'uncatalyzed' reaction rates[1]. At 0.5 mM Fe(II), SO_2 oxidation rates are on the order of 10^{-6} M/s. In the presence of the roughly 0.1-0.5M Fe(II) that may be present during olivine leaching in SO_2, it is likely that aerobic oxidation will be rapid, even upwards of 10^{-3} M/s. Therefore, to minimize deleterious loss of SO_2 by oxidation to sulfate, it is critical to remove oxygen prior to leaching and release of Fe(II). We envision that during the proposed process, the most significant source of oxygen introduction will be during olivine addition and makeup water addition prior to leaching. Solid additions could be purged through vacuum-cycle or pressure-cycle purging[2]. Dissolved oxygen in water may be purged through dilution purging with N_2, but this adds further operating costs. The solubility of oxygen in water at ambient conditions is around 1 mM[3]. Since there is roughly 1-2M concentration of SO_2 in solution at 1 atm[4,5], even in the absence of any purging, stoichiometric reaction of dissolved oxygen would lead to just ~0.1% of all the introduced SO_2 being oxidized to sulfate. A complete technoeconomic analysis on the tradeoff of SO_2 loss to sulfate as compared to purging requirements is beyond the scope of this work but will be the focus of future studies.

2. Determination of percent pyroxene in olivine

The pXRD pattern of the olivine starting material matches olivine (Mg_2SiO_4) closely, with additional peaks at 28.3° and 31.1° that match with the strongest peak in the pyroxene ($MgSiO_3$) reference pattern (**Fig. S1**). Therefore, we assumed that the starting material was a mixture of olivine and pyroxene. We could not confidently assign the weak peaks at 12.1° and 30.3°, indicating the presence of a small quantity of an unknown impurity. To estimate the amount of pyroxene present, we assumed a 92.5:7.5 ratio of Mg:Fe. This value was chosen because the observed percent Mg^{2+} (i.e. $[Mg^{2+}]/([Mg^{2+}] + [Fe^{2+}])$) was 92.5 ± 0.5 % throughout dissolution of the starting material in both HNO_3 and SO_2. Utilizing this assumption, the molecular weight of olivine is (140.69 * 0.925) + (203.77 * 0.075) = 145.42 g/mol. Similarly, the molecular weight or pyroxene is (100.39 * 0.925) + (131.93 * 0.075) = 102.76 g/mol. We then measured the total amount of Mg^{2+} and Fe^{2+} released from the starting material at complete dissolution. Dissolution was determined to be complete after 13 hours in 1M HNO_3 at 80 °C, when the change in Mg^{2+} and Fe^{2+} concentration was less than 1% over 90 minutes. We observed that 0.0358 g of starting material led to the formation of 0.455 mmol of M^{2+} (Mg^{2+} and Fe^{2+}). From this endpoint concentration, we determined that the 'molecular weight' of the starting material, in terms of grams per mole M^{2+}, is 78.6 g/mol M^{2+}. Converting the molecular weights of olivine and pyroxene to these units gives 72.71 g/mol M^{2+} (dividing 145.42 g/mol by 2 to account for the cation stoichiometry) and 102.76 g/mol M^{2+}, respectively. Thus, we can determine the % pyroxene from equation S1.

$$x(102.76) + (1 - x)(72.71) = 78.6 \qquad (S1)$$

Where x is the fraction of M^{2+} from pyroxene. Solving the expression yields 0.196, so we estimate the percent M^{2+} from pyroxene as roughly 19.6% with 80.4% M^{2+} from olivine.

3. Discussion of Idealized Pressure – Solubility – pH relationship

To calculate the idealized pressure-solubility-pH relationship, we considered the following equilibrium relationships: the first and second acid dissociation constants for SO_2, charge balance, and solubility constants for a variety of different regimes. In all the subsequent discussion, we assume that activity coefficients are equal to 1, therefore activities will be represented as concentrations. We also assume the activity of water is 1, and will be ignored in the subsequent calculations. We also assume that solid solutions are not formed. At the high concentrations (>1 M) used in these studies, these are erroneous assumptions for our measured conditions, but are necessary to simplify analysis.

3.1 Pressure-pH relationship in the absence of any precipitating solid.

The following analysis considers the case where $MgSO_3$ is completely dissolved, forming a $Mg(HSO_3)_2$ solution, and we considered the following equilibrium relationships (**S2**, **S3**), and the charge balance relationship (**S4**)

$$SO_{2(g)} + H_2O_{(l)} \rightleftharpoons H^+_{(aq)} + HSO^-_{3\,(aq)}$$

$$K_{a1} = \frac{[H^+][HSO_3^-]}{P_{SO2}a_{H2O}} \qquad (S2)$$

$$HSO^-_{3(aq)} \rightleftharpoons H^+_{(aq)} + SO^{2-}_{3\,(aq)}$$

$$K_{a2} = \frac{[H^+][SO_3^{2-}]}{[HSO_3^-]} \qquad (S3)$$

$$[H^+] + 2[Mg^{2+}] = [HSO_3^-] + 2[SO_3^{2-}] \qquad (S4)$$

We take $K_1 = 10^{-1.8}$, $K_2 = 10^{-7}$.[6] The water activity is taken as unity and ignored in subsequent derivations. Note that the charge balance expression **S4** is established such that each Mg^{2+} represents a MgO equivalent, rather than Mg^{2+} in the absence of alkalinity (e.g. $MgCl_2$, see below). We aim to solve this system of equations by deriving an expression in terms of $[Mg^{2+}]$ and P_{SO2}.

Rearranging **S2** yields

$$[HSO_3^-] = \frac{K_{a1}P_{SO2}}{[H^+]} \qquad (S5)$$

Rearranging **S3** and substituting **S5** yields

$$[SO_3^{2-}] = \frac{K_{a2}[HSO_3^-]}{[H^+]} = \frac{K_{a1}K_{a2}P_{SO2}}{[H^+]^2} \qquad (S6)$$

Substituting **S5** and **S6** into **S4** and multiplying by $[H^+]^2$ yields

$$[H^+]^3 + 2[Mg^{2+}][H^+]^2 - K_{a1}P_{SO}\ [H^+] - 2K_{a1}K_{a2}P_{SO}\ = 0 \qquad (S7)$$

By varying $[Mg^{2+}]$ and P_{SO2} as parameters, Equation S7 can be solved for $[H^+]$ as a function of $[Mg^{2+}]$ and P_{SO2}. There are three solutions, and we take the largest positive solution as the chemically meaningful solution. Plotting these results as a graph of pH vs log(P) allows us to extract the dependence of pH on pressure from a linear fit (**Fig. S14a**).

From this analysis, we calculate that between 0.001 and 10 atm SO_2, there is an inverse 1st order dependence of pH on SO_2 pressure when the concentration of Mg^{2+} is greater than 0.25M. This decreases slightly to an inverse 0.91 order at 0.1M Mg^{2+}, which is the result of curvature at high pressure (**Fig. S14a, red**). Finally, there is an inverse 0.5 order in the absence of any Mg^{2+}. This can be understood intuitively by analysis of the extrema. In the absence of any Mg^{2+}, the change in pH with change in SO_2 pressure is analogous to the dissociation of any other weak acid. In this case, **S4** indicates that $[H^+] = [HSO_3^-]$. This means that in **S2**, changes in SO_2 pressure will result in equal changes in $[H^+]$ and $[HSO_3^-]$ to maintain the equilibrium relationship. Thus, changes in SO_2 pressure are diluted into changing both $[H^+]$ and $[HSO_3^-]$, resulting in the smaller inverse 0.5 order dependence on pressure. In contrast, at high $[Mg^{2+}]$, **S4** indicates that $2[Mg^{2+}] \approx [HSO_3^-]$. This means that in **S2**, $[HSO_3^-]$ will be substantially larger than $[H^+]$. Thus, changes in SO_2 pressure will change $[H^+]$ and $[HSO_3^-]$ by a similar amount on an absolute scale, but will change $[H^+]$ by a much larger amount on a relative scale. As a result, the equilibrium relationship **S2** will be much more sensitive to changes in $[H^+]$, resulting in the larger inverse 1st order dependence of pH on SO_2 pressure in the presence of an excess of MgO equivalents.

We also use this analysis to calculate the relationship between P_{SO2} and $[SO_3^{2-}]$ **(Fig. S14b)**. We observe that at high concentrations of Mg^{2+} (1M), the relationship is inverse first order. At the other extreme, of 0 M Mg^{2+}, there is a near zero relationship between P_{SO2} and $[SO_3^{2-}]$. At concentrations of Mg^{2+} between these two extremes, the relationship shifts as a function of pressure, approaching inverse first order at low pressures of SO_2 and larger $[Mg^{2+}]$.

From these calculated speciation curves, we conclude that in the absence of Mg^{2+} (specifically MgO equivalents or alkalinity), decreasing the pressure of SO_2 does not increase $[SO_3^{2-}]$. However, even at just 0.01 M Mg^{2+}, the inverse relationship between SO_2 pressure and $[SO_3^{2-}]$ becomes apparent. This relationship can be understood intuitively by considering the autoprotolysis reaction of HSO_3^-.

$$2HSO_{3\,(aq)}^- \rightleftharpoons SO_{2(g)} + SO_{3\,(aq)}^{2-} + H_2O_{(l)}$$

$$\frac{K_{a2}}{K_{a1}} = \frac{P_{SO2}[SO_3^{2-}]a_{H2O}}{[HSO_3^-]^2} \qquad (S8)$$

Changes in SO_2 pressure will result in roughly equal changes in $[SO_3^{2-}]$ and $[HSO_3^-]$ in absolute terms, but the relative magnitude of $[HSO_3^-]$, $[SO_3^{2-}]$, and P_{SO2} will determine which species experiences the largest relative change in concentration. In the presence of high $[Mg^{2+}]$, where $[HSO_3^-]$ is pinned by $2[Mg^{2+}] \approx [HSO_3^-]$, as shown in **S4**, changes in SO_2 pressure result in negligible change in $[HSO_3^-]$, on a relative scale Thus, changes in P_{SO2} will be matched with commensurate changes in $[SO_3^{2-}]$ in order to maintain the equilibrium relationship set by **S8.** In contrast, in the absence of $[Mg^{2+}]$, $[HSO_3^-]$ is not substantially larger than P_{SO2} and $[SO_3^{2-}]$ and as SO_2 pressure is modulated, the relative change in $[SO_3^{2-}]$ is diluted as $[HSO_3^-]$

changes more dramatically. Indeed, between 0.001 and 10 atm SO_2, $[HSO_3^-]$ changes by 99% in the absence of Mg^{2+}, and changes just 6% in the presence of 1 M Mg^{2+}.

To determine the role of alkalinity in allowing increases in $[SO_3^{2-}]$ with a decrease in SO_2 pressure, we can also compare the case described above to a scenario where Mg^{2+} is introduced as $MgCl_2$. In that instance, the charge balance relationship is altered to be

$$[H^+] + 2[Mg^{2+}] = [HSO_3^-] + 2[SO_3^{2-}] + [Cl^-] \quad (S9)$$

However, since

$$2[Mg^{2+}] = [Cl^-] \quad (S10)$$

the charge balance relationship becomes

$$[H^+] = [HSO_3^-] + 2[SO_3^{2-}] \quad (S11)$$

indicating that Mg^{2+} in the absence of alkalinity will result in a scenario like that described above when no $Mg(HSO_3)$ is present. In other words, in the absence of alkalinity, decreasing SO_2 pressure will not modulate $[SO_3^{2-}]$ substantially, and the observed utility in decreasing pressure for driving sulfite precipitation is lost. This can be understood intuitively by recognizing that to generate alkaline conditions with high $[SO_3^{2-}]$ by reducing SO_2 pressure, alkalinity must be present prior to the addition of SO_2. In the absence of initial alkalinity, alkalinity cannot be generated simply by removing the acidic SO_2 species. As a result, only alkaline mixtures can be directly separated using the pressure swing process (i.e. oxides, carbonates, silicates, phosphates, etc.). To allow for pressure-swing separation of metal chlorides, for example, a source of alkalinity must be provided (e.g. NaOH).

3.2. Pressure-pH relationship in the presence of a single precipitating sulfite.

The following analysis considers the case where $MgSO_3$ can precipitate and is in equilibrium with a $Mg(HSO_3)_2$ solution. We considered the following equilibrium relationships **S12, S13, S15**, and the charge balance relationship **S14**.

$$SO_{2(g)} + H_2O_{(l)} \rightleftharpoons H^+_{(aq)} + HSO^-_{3\,(aq)}$$

$$K_{a1} = \frac{[H^+][HSO_3^-]}{P_{SO}\ a_{H2O}} \quad (S12)$$

$$HSO^-_{3(aq)} \rightleftharpoons H^+_{(aq)} + SO^{2-}_{3\,(aq)}$$

$$K_{a2} = \frac{[H^+][SO_3^{2-}]}{[HSO_3^-]} \quad (S13)$$

$$[H^+] + 2[Mg^{2+}] = [HSO_3^-] + 2[SO_3^{2-}] \quad (S14)$$

$$MgSO_{3(s)} \rightleftharpoons Mg^{2+}_{(aq)} + SO_3^{2-}{}_{(aq)}$$
$$K_{sp,Mg} = [Mg^{2+}][SO_3^{2-}] \quad (S15)$$

We take $K_1 = 10^{-1.8}$, $K_2 = 10^{-7}$, $K_{sp,\,Mg} = 10^{-3}$. The water activity is taken as unity and ignored in subsequent derivations.

To solve this system of equations, we express $[H^+]$, $[HSO_3^-]$, and $[SO_3^{2-}]$ in terms of $[Mg^{2+}]$, then substitute into **S14**.

Rearranging **S13** and **S15** yields

$$[SO_3^{2-}] = \frac{K_{a2}[HSO_3^-]}{[H^+]} = \frac{K_{sp,Mg}}{[Mg^{2+}]} \quad (S16)$$

Rearranging the two righthand terms in **S16** yields

$$[HSO_3^-] = \frac{[H^+]K_{sp,Mg}}{K_{a2}[Mg^{2+}]} \quad (S17)$$

Recalling **S5**

$$[HSO_3^-] = \frac{K_{a1}P_{SO2}}{[H^+]} \quad (S18)$$

Substituting **S18** into **S17** yields

$$[H^+] = \sqrt{\frac{K_{a1}P_{SO2}K_{a2}}{K_{sp,Mg}}}[Mg^{2+}]^{0.5} \quad (S19)$$

Substituting **S19** into **S18** yields

$$[HSO_3^-] = \sqrt{\frac{K_{a1}P_{SO2}K_{sp,Mg}}{K_{a2}}}[Mg^{2+}]^{-0.5} \quad (S20)$$

Substituting the expressions for $[H^+]$, $[HSO_3^-]$, and $[SO_3^{2-}]$ (**S16, S19, S20**) into **S14** and multiplying by $[Mg^{2+}]$ yields the following expression in terms of $[Mg^{2+}]$ and P_{SO2}

$$2[Mg^{2+}]^2 + \sqrt{\frac{K_{a1}P_{SO2}K_{a2}}{K_{sp,Mg}}}[Mg^{2+}]^{1.5} - \sqrt{\frac{K_{a1}P_{SO}\ K_{sp,Mg}}{K_{a2}}}[Mg^{2+}] - 2K_{sp,Mg} = 0 \quad (S21)$$

To solve for $[Mg^{2+}]$, we perform a substitution $t = \sqrt{[Mg^{2+}]}$ so that we can generate a quartic equation. Then, we vary P_{SO2} as a parameter and take the largest positive real solution as the chemically meaningful one. Plotting $\log(P_{SO2})$ versus $\log[Mg^{2+}]$ (**Fig. S14c**), we calculate a slope of 0.33. In other words, an order of magnitude decrease in SO_2 pressure leads to a third of an order of magnitude decrease in Mg^{2+} concentration.

We can also solve for an expression in terms of $[H^+]$ by substituting **S19** into **S21**, which gives

$$\frac{2K_{sp,Mg}}{K_{a1}K_{a2}P_{SO2}}[H^+]^4 + [H^+]^3 - K_{a1}P_{so2}[H^+] - 2K_{a1}K_{a2}P_{SO2} = 0 \qquad (S22)$$

Again, we take the largest, real, positive solution. Plotting pH versus $\log(P_{SO2})$ (**Fig. S14d**), we observe a slope of −0.66. In other words, for every decade decrease in SO_2 pressure, there is a two thirds order of magnitude increase in pH. Intuitive understanding of the exact scaling of pH and $[Mg^{2+}]$ as a function of SO_2 pressures is difficult. However, the attenuated scaling compared to the non-precipitating scenario in **Supplementary Note 2.1** can be understood, by recognizing that precipitation of the solid sulfite leads to removal of SO_3^{2-} species from the aqueous solution, thereby diminishing the increase in alkalinity that occurs with SO_2 pressure reduction.

3.3. Pressure-pH relationship in the presence of a precipitating sulfite and a non-precipitating cation.

The following analysis considers the case where $FeSO_3$ can precipitate and is in equilibrium with an $Fe(HSO_3)_2$ solution, and a $Mg(HSO_3)_2$ solution is present but $MgSO_3$ does not precipitate. We considered the following equilibrium relationships

$$SO_{2(g)} + H_2O_{(l)} \rightleftharpoons H^+_{(aq)} + HSO^-_{3\,(aq)}$$
$$K_{a1} = \frac{[H^+][HSO_3^-]}{P_{SO2}a_{H2O}} \qquad (S23)$$

$$HSO^-_{3(aq)} \rightleftharpoons H^+_{(aq)} + SO^{2-}_{3\,(aq)}$$
$$K_{a2} = \frac{[H^+][SO_3^{2-}]}{[HSO_3^-]} \qquad (S24)$$

$$[H^+] + 2[Fe^{2+}] + 2[Mg^{2+}] = [HSO_3^-] + 2[SO_3^{2-}] \qquad (S25)$$

$$FeSO_{3(s)} \rightleftharpoons Fe^{2+}_{(aq)} + SO^{2-}_{3\,(aq)}$$
$$K_{sp,Fe} = [Fe^{2+}][SO_3^{2-}] \qquad (S26)$$

We take $K_1 = 10^{-1.8}$, $K_2 = 10^{-7}$, $K_{sp,Fe} = 10^{-5}$. The water activity is taken as unity and ignored in subsequent derivations.

To solve this system of equations, we express $[H^+]$, $[HSO_3^-]$, and $[SO_3^{2-}]$ in terms of $[Fe^{2+}]$, then substitute into **S25**.

Rearranging **S24** and **S26** yields

$$[SO_3^{2-}] = \frac{K_{a2}[HSO_3^-]}{[H^+]} = \frac{K_{sp,Fe}}{[Fe^{2+}]} \quad (S27)$$

Rearranging the two righthand terms in **S27** yields

$$[HSO_3^-] = \frac{[H^+]K_{sp,Fe}}{K_{a2}[Fe^{2+}]} \quad (S28)$$

Recalling **S5**

$$[HSO_3^-] = \frac{K_{a1}P_{SO2}}{[H^+]} \quad (S29)$$

Substituting **S29** into **S28** yields

$$[H^+] = \sqrt{\frac{K_{a1}P_{SO}\ K_{a2}}{K_{sp,Fe}}}[Fe^{2+}]^{0.5} \quad (S30)$$

Substituting **S30** into **S29** yields

$$[HSO_3^-] = \sqrt{\frac{K_1P_{SO}\ K_{sp,Fe}}{K_2}}[Fe^{2+}]^{-0.5} \quad (S31)$$

Substituting the expressions for $[H^+]$, $[HSO_3^-]$, and $[SO_3^{2-}]$ (**S27, S30, S31**) into **S14** and multiplying by $[Fe^{2+}]$ yields the following expression in terms of $[Mg^{2+}]$, $[Fe^{2+}]$, and P_{SO2}

$$2[Fe^{2+}]^2 + \sqrt{\frac{K_{a1}P_{SO2}K_{a2}}{K_{sp,Fe}}}[Mg^{2+}]^{1.5} - \sqrt{\frac{K_{a1}P_{SO2}K_{sp,Fe}}{K_{a2}}}[Mg^{2+}] - 2K_{sp,Fe} = 0 \quad (S32)$$

To solve for $[Fe^{2+}]$, we set $t = \sqrt{[Fe^{2+}]}$ so that we generate a quartic equation. Then, we vary $[Mg^{2+}]$ and P_{SO2} as parameters and take the largest positive real solution as the chemically meaningful one.

Plotting $\log(P_{SO2})$ versus $\log[Fe^{2+}]$ (**Fig. S14e**), we observe that the slope changes from near 1 at high concentrations of Mg^{2+} (2M Mg^{2+}), to a slope near 0.33 for low concentrations of Mg^{2+} (0.01M Mg^{2+}). In

the limit of low concentrations of Mg^{2+}, this regime begins to resemble that of **S3.2,** with only a single precipitating solid, where the order is also 0.33. In the limit of high Mg^{2+} concentrations, the change in $[SO_3^{2-}]$ appear to be dominated by the presence of aqueous Mg^{2+}, and begins to mirror that of **S3.1**, which contains no solid precipitates. In that regime, there is a first order relationship between P_{SO2} and $[SO_3^{2-}]$. This then leads to the first order relationship between P_{SO2} and $[Fe^{2+}]$, since $[Fe^{2+}]$ and $[SO_3^{2-}]$ are related through $K_{sp,Fe}$.

4. Gibbs Phase Rule Analysis

Gibbs Phase Rule states that the degrees of freedom (F) in a system at equilibrium is defined by

$$F = C - P + 2$$

where C is the number of components, and P is the number of phases[7]. In the MgO-FeO-SO_2-H_2O system described here, there are 4 components, and 3 phases (gas, aqueous, and solid solution). As a result, 3 independent variables must be defined to uniquely determine the system. In this case, we chose to use 3 easily measurable independent variables ($[M^{2+}]$, Fe^{2+} aqueous fraction, temperature). Thus, if these three independent variables are defined, then we can be confident that the SO_2 pressure is uniquely prescribed.

pXRD evidence (**Fig. S12**) indicates that near a 50/50 ratio of Mg^{2+}/Fe^{2+} there is a miscibility gap and the presence of two solid phases. This will reduce the degrees of freedom by one, but as this reduces the required number of variables to assign the equilibrium SO_2 pressure without ambiguity, this is inconsequential.

5. Interpolation of log($[M^{2+}]$)-log($P(SO_2)$)-Fe^{2+} aqueous Fraction Data

To calculate the SO_2 pressures that would be in equilibrium with the $[M^{2+}]$ and Fe^{2+} aqueous fractions determined based on the countercurrent analysis, we needed to interpolate the measured data such that a wide variety of possible $[M^{2+}]$ and Fe^{2+} aqueous fractions could be analyzed. While an ideal system with aqueous and solid solution activity coefficients equal to 1 could be fit with meaningful parameters, we found that the non-idealities at high concentrations made this unfeasible, and the number of parameters necessary to account for the unknown activity coefficients was untenable. As a result, we applied a purely empirical fit, chosen only for its ability to effectively fit the data within the measured range while retaining p-values far below 0.05.

$$\log([M^{2+}]) = a + (b * \log(P) + c) * \left(Fe^{2+}_{aq,fraction}\right)^{0.5} + d * \log(P) \qquad (S33)$$

The form of the expression was chosen by analyzing the general form log($[M^{2+}]$)-log($P(SO_2)$)-Fe^{2+} aqueous fraction data in two dimensions at a time. As an example, at a fixed Fe^{2+} fraction, the relationship between log$[M^{2+}]$ and log(P) is roughly linear, motivating the use of a linear function to describe the relationship between log$[M^{2+}]$ and log(P). This led us to use the $b * \log(P)$ and $d * \log(P)$ terms. However, the slope of that linearity changes as a function of Fe^{2+} fraction, motivating the coefficient for the slope of the log$[M^{2+}]$ − log(P) curve to be dependent on Fe^{2+} fraction. This led us to use the $(b * \log(P) + c) * \left(Fe^{2+}_{aq,fraction}\right)^{0.5}$ term, which allows the slope of the log$[M^{2+}]$ and log(P) relationship to vary with Fe^{2+} fraction. The 0.5 exponent is present because the rate at which the slope of the log$[M^{2+}]$ and log(P) relationship changes is not constant with changing Fe^{2+} fraction. Using the expression above, experimental solubility data was fit, yielding parameters a = 0.3401, b = 0.1172, c = −0.5851, d = 0.1589. The fit yields a Coefficient of Determination of 0.985. To estimate the error from this interpolation, we performed a

procedure wherein we randomly removed 15% (8 values) of the data points to serve as a testing set, then performed the fit again, then used the new fit to attempt to predict the value of the testing set. The parameters for the fits with points removed were typically within 2% of the values with all the data points, and never more than 5% different. Finally, we complied the errors for three testing sets, and found that the average error in $\log([M^{2+}])$ was 0.01816, similar to our experimental error of 0.0178. We wish to clearly state that chemical meaning should not be ascribed to the parameters, nor should this fit be utilized outside of the range of the data.

6. Discussion on $MgSO_3$ Calcination

When performing $MgSO_3$ calcinations under inert atmosphere in quartz tubes, we observed the deposition of fine white-yellow particulates on the inner wall of the quartz. These fine particulates would melt and recrystallize into larger yellow crystals when exposed to a low temperature (100-300 °C) heat gun. Based on these observations, and the observation of $MgSO_4$ in the pXRD product during $MgSO_3$ calcination at temperatures between 800-900 °C, we concluded, as has been observed before, that gaseous sulfur forms as an intermediate kinetic product during $MgSO_3$ calcination through sulfur disproportionation to S(0) and S(VI)[8–10]. While not inherently problematic, if sulfur gas is entrained in gas flow and is unable to react with $MgSO_4$ to form MgO and SO_2, this will increase the heat requirement for the decomposition[11,12]. As a result, we conclude that appropriate gas-solid mass transport regimes must be ensured during calcination to avoid separation of S(0) and S(VI) intermediates prior to their comproportionation. Indeed, we observe that when a bed of $MgSO_3 \cdot 3H_2O$ particles is calcined at 890 °C, the interior of the bed showed notably more $MgSO_4$ in the final solid product as opposed to the exterior of the bed (**Fig. S19**). We hypothesize that this is due to a longer residence time of sulfur gas with the exterior of the bed as it diffuses out of the bed after formation in the interior of the bed. While the development of an optimal reactor design for $MgSO_3$ calcination is beyond the scope of this work, our preliminary results indicate that maximizing gas-solid residence time to avoid elemental sulfur loss and concurrent $MgSO_4$ formation is of utmost importance.

7. Discussion on Gas Management

The proposed approach will inevitably require careful control of gases to be performed effectively at large-scale. While a detailed technoeconomic analysis is beyond the scope of this work and is the focus of future research, we offer here a few notes on potential methods of gas separation.

We envision that separation of SO_2 from air and from inert (likely N_2) are most likely to be important in recycling SO_2. This will be particularly true if N_2 is used to purge reactions to either decrease SO_2 pressure during precipitation or calcination, or if air is used during solid calcination. SO_2 liquefaction is the most viable mode of separation because of the much higher boiling point of SO_2 (−10°C)[13] as compared to N_2(−196°C) and O_2(−183°C)[14]. However, if SO_2 is diluted too much, the required temperatures for condensation may become exceedingly low. Among industrially practiced SO_2 separation and concentration approaches[15], the Linde Solinox process[16] and the Wellman-Lord process[17] have demonstrated particular effectiveness.

8. Discussion on Calculated Enthalpic Cost

8.1. Minimum Enthalpic Cost for Chemical Reactions

For thermodynamic calculations of minimum enthalpic cost, we used the following literature values[18] of standard enthalpy of formation, $\Delta H_f°$: Mg_2SiO_4: −2174 kJ/mol; SO_2: −296 kJ/mol; H_2O(liquid): −285 kJ/mol; H_2O(gas): −241 kJ/mol; Mg^{2+}: −466 kJ/mol; HSO_3^-: −626 kJ/mol; SiO_2(am): −903 kJ/mol;

$MgSO_3 \cdot 3H_2O$: −1932 kJ/mol; MgO: −601 kJ/mol; $NO_2(g)$: 33 kJ/mol; $O_2(g)$: 0 kJ/mol; NO_3^-: −205 kJ/mol; $Mg(NO_3)_2 \cdot 6H_2O$: −2613 kJ/mol (**Table S1**). Values in Main Text are reported to 10s kJ/mol.

The chemical equations that are not explicitly written in the main text are as follows:

Water Condensation:

$$H_2O(g) \rightarrow H_2O(l) \quad (S34)$$

$\Delta H° = -44$ kJ/mol

Water Evaporation:

$$H_2O(l) \rightarrow H_2O(g) \quad (S35)$$

$\Delta H° = 44$ kJ/mol

In estimating the cost of evaporating water to form $Mg(NO_3)_2 \cdot 6H_2O$, we assume that at 4 M Mg^{2+}, there are 13.87 moles of water per mole of Mg, assuming 55.55 mol H_2O/L.

The series of chemical equations considered in evaluating the nitrate looping process are as follows:

Leaching:

$$½\, Mg_2SiO_4 + 2NO_2 + \frac{1}{2}O_2 \rightarrow Mg^{2+} + 2NO_3^- + ½\, SiO_2 \quad (S36)$$

$\Delta H° = -306$ kJ/mol

Precipitation:

$$Mg^{2+} + 2NO_3^- + 6H_2O(l) \rightarrow Mg(NO_3)_2 \cdot 6H_2O \quad (S37)$$

$\Delta H° = -27$ kJ/mol

Evaporation:

$$H_2O(l) \rightarrow H_2O(g) \quad (S38)$$

$\Delta H° = 44$ kJ/mol

Calcination:

$$Mg(NO_3)_2 \cdot 6H_2O \rightarrow MgO + 2NO_2 + 6H_2O(g) + \frac{1}{2}O_2 \quad (S39)$$

$\Delta H° = 632$ kJ/mol

The endothermic costs of the nitrate looping process are summed to estimate the total energy input requirement of 1242 kJ/mol, as shown in **Table 2**.

8.2. Minimum Enthalpic Cost for Gas Pressurization

To estimate the cost of SO_2 gas pressurization, we assumed SO_2 behaves as an ideal gas and used the following expression to estimate the work required for isothermal compression:

$$W = nRTln\left(\frac{P_2}{P_1}\right) \quad (S40)$$

Where n is 2, an estimate for the number of moles of SO_2 required to process one mole of Mg^{2+}, R is the universal gas constant, or 0.008314 kJ mol^{-1} K^{-1}, T is the temperature, 298 K, and P_2 and P_1 are the final and initial gas pressures, respectively. Taking an extreme condition of requiring 5 orders of magnitude change in pressure, this gives a value of 57 kJ/mol Mg.

Supplementary Figures

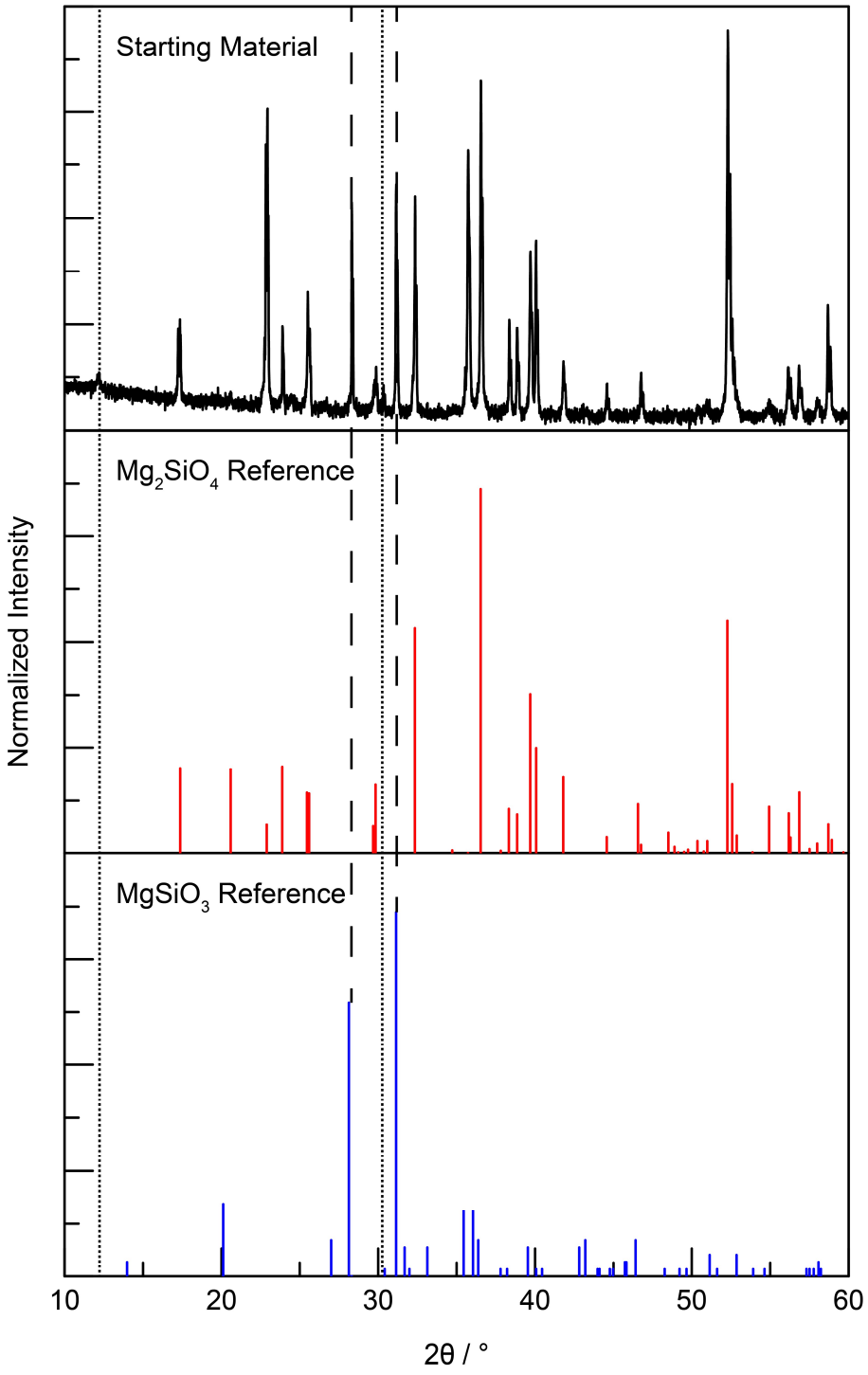

Fig. S1. X-ray diffraction patterns of starting material. Measured PXRD pattern of the olivine starting material (black) with reference patterns for Mg_2SiO_4 (red) and $MgSiO_3$ (blue). The dashed lines indicate peaks assigned to $MgSiO_3$, while the dotted lines indicate unidentified peaks. Performed with a Cu X-ray source.

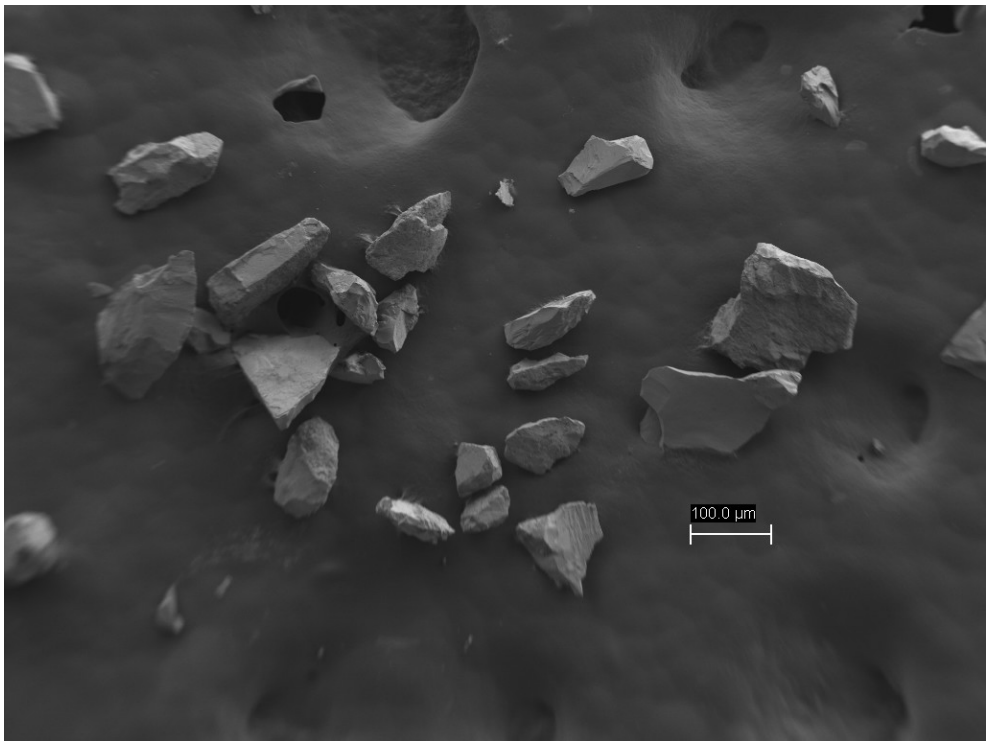

Fig. S2. SEM micrograph of starting material. SEM Micrograph of the olivine starting material. Samples were prepared by dispersing dry particles on carbon tape. An accelerating voltage of 1.00 kV was used. We observe that particles have sizes roughly matching the expected 32-212 µm expected based on the sieving procedure we employed. In addition, the particle faces do not appear to have fine particles adsorbed onto their surfaces.

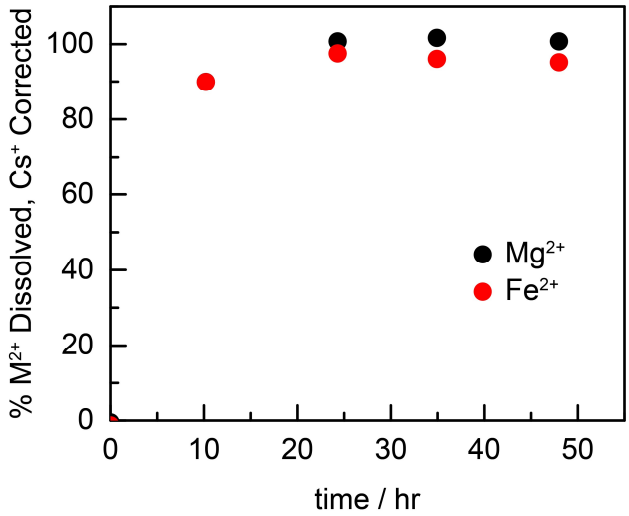

Fig. S3. **Dissolved ion concentrations during long-duration SO_2 leach of olivine.** Measured percent dissolution of Mg^{2+} (black) and Fe^{2+} (red) over time during dissolution of olivine in 3.5 atm SO_2, 80 °C, 15% solids by mass. The percent dissolution is calculated from the measured moles M^{2+} released during long term nitric acid leaching per gram of olivine. The measured concentrations of Mg^{2+} and Fe^{2+} are also corrected to account for the volume expansion upon SO_2 introduction through the use of a Cs^+ internal standard (see Methods).

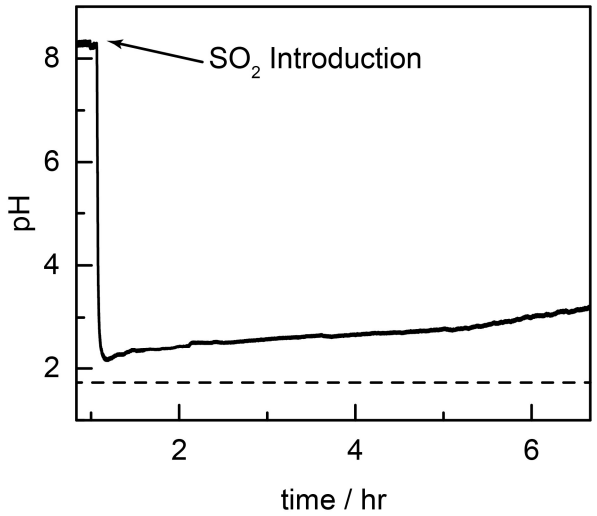

Fig. S4. Measured pH during 1 atm SO_2 olivine leaching. Measured pH during olivine leaching at 0.53 atm SO_2, 80 °C, 18% solids by mass. The dotted black line indicates the measured pH (1.73) of water exposed to 0.53 atm SO_2, 80 °C, in the absence of olivine.

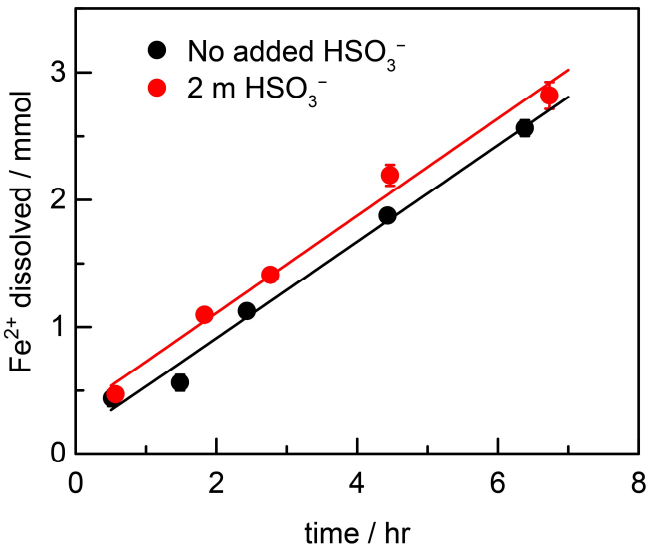

Fig. S5. Effect of bisulfite concentration on olivine leaching rates in SO_2. Measured moles of Fe^{2+} leached over time during dissolution of olivine in 2.96 atm SO_2, 40 °C, 6.7% solids by mass in the presence (red) and absence (black) of 2 m $Mg(HSO_3)_2$. The 2 m $Mg(HSO_3)_2$ solution was generated by the addition of $Mg(OH)_2$, which dissolved rapidly to form $Mg(HSO_3)_2$. The black and red line represent the linear best fits to the black and red data points, respectively. The slopes are 0.379 and 0.347 mmol/hr, respectively. Measured concentrations were corrected for volume expansion upon exposure to SO_2 and dissolution on Mg^{2+} by use of the Cs^+ internal standard method (see Methods). Fe^{2+} concentrations are used to deduce dissolution the rate to avoid convolution from the added $Mg(OH)_2$. The data presented in red is the average of two trials, with error bars indicating the range between the two trials. The data presented in black is a single trial, with error bars indicating the error in the dilution and ICP-OES measurement. When error bars are not visible they are smaller than the size of the data points.

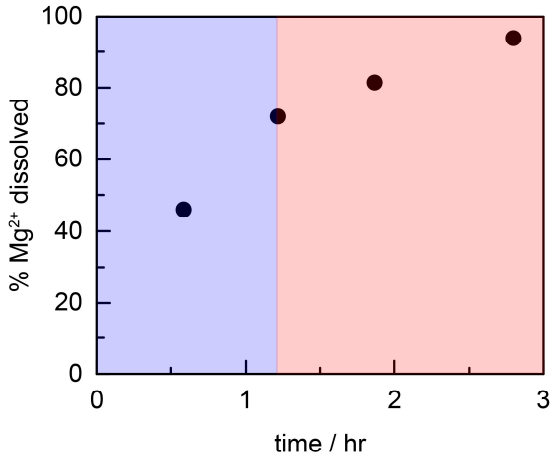

Fig. S6. Effect of particle reactivity on dissolution rates in the absence of pH changes. Measured percent dissolved Mg^{2+} over time during dissolution of olivine in 1M HNO_3, 80°C, 0.3% solids by mass. Over the first 1.2 hours (blue section), 72% of the Mg^{2+} dissolved, while in the subsequent 1.53 hours (red section), 22.0% of the Mg^{2+} dissolved. Estimating the rates as linear in those time periods, we calculate that the rates are about 4.11 times faster during the initial 70% dissolution than the subsequent 20% dissolution.

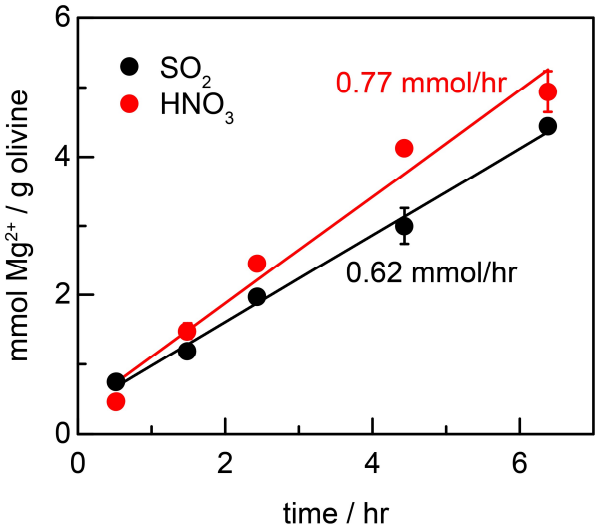

Fig. S7. Comparison of olivine leaching rates in HNO_3 and SO_2 at common acid concentrations. Measured moles of Mg^{2+} dissolved per gram of olivine over time during dissolution of olivine in 2.44 m SO_2 (black) and 2.48 m HNO_3 (red), 40 °C, 6.7% solids by mass. To achieve 2.44 m SO_2, a partial pressure of 2.96 atm SO_2 is maintained. The measured concentrations for the SO_2 leach are corrected for volume expansion of the solution through use of a Cs^+ internal standard (see Methods). The data presented are the average of two identical trials, with the error bars indicating the range between the two trials. In cases where the error bars are not visible, they are smaller than the size of the data point marker. The lines represent linear best fits, with the slopes of each line indicated in the corresponding color.

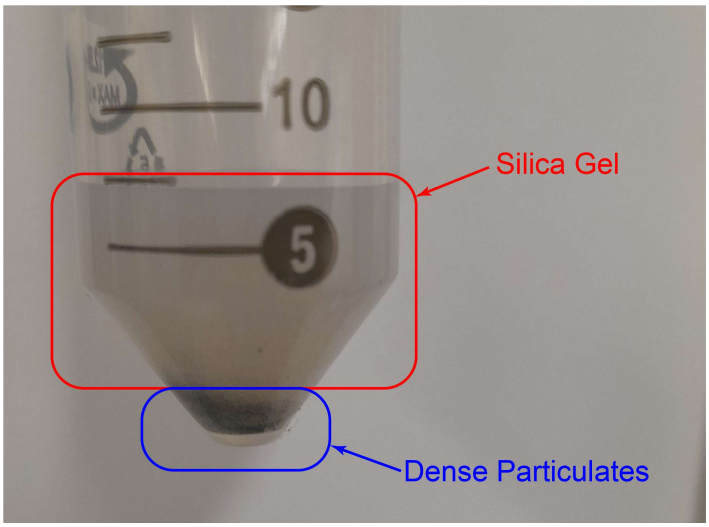

Fig. S8. Photograph of silica formed from SO_2 leaching of olivine. Optical photograph of solid residue after dissolution of olivine in 3.5 atm SO_2, 80 °C, 15% solids by mass, for 48 hours. After leaching, the solid product was separated by centrifugation, then rinsed with water 4 times, separating each rinse solution by centrifugation. The labeled components of the photograph indicate the decanted silica gel and the remaining dense particulates.

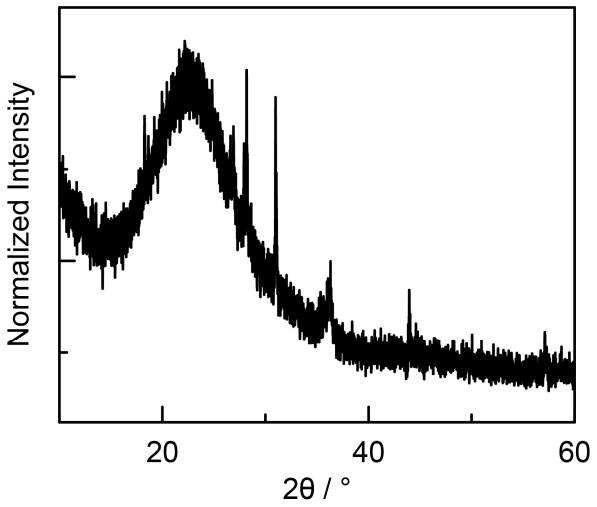

Fig S9. X-ray diffraction pattern of dense black particulates in olivine after SO_2 leaching. PXRD of black particulate layer of the leach product, after a 48-hour dissolution of olivine in 3.5 atm SO_2, 80 °C, 15% solids by mass. Performed with a Cu X-ray source.

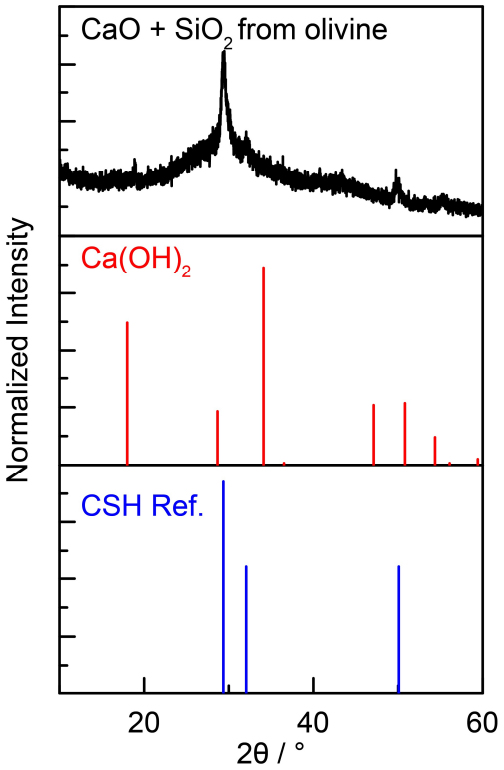

Fig. S10. X-Ray diffraction pattern of cementitious calcium silicate hydrates formed from olivine-derived silica. PXRD of gelatinous product generated from exposing CaO to the SiO_2 generated from olivine leaching in water at room temperature for 23 hours (black) along with the $Ca(OH)_2$ (red), and calcium silicate hydrate (CSH) (blue) reference patterns. Performed with Cu X-ray source.

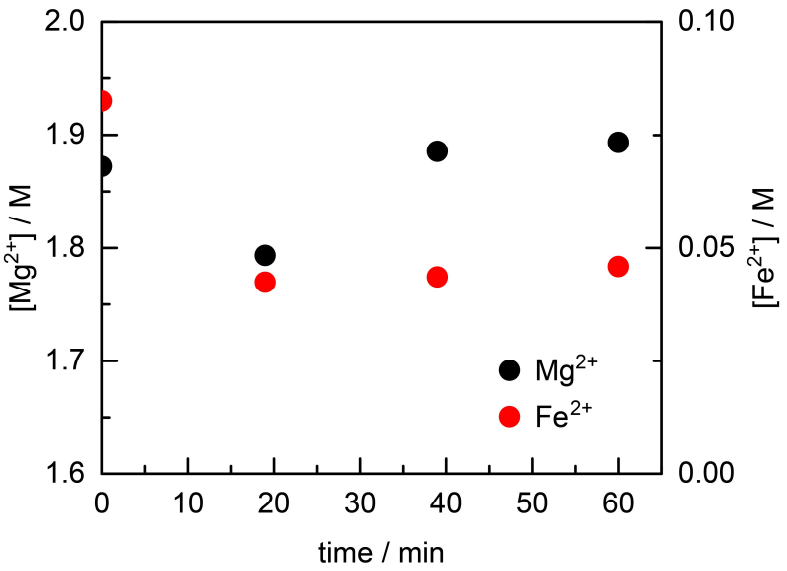

Fig. S11. Measured time for solid-liquid equilibration after pressure modulation. Measured concentration of Mg^{2+} and Fe^{2+} over time upon reducing the SO_2 pressure from 3.18 atm to 1.75 atm at time = 0. Pressure reduction was performed in less than one minute. Data collected at 80 °C.

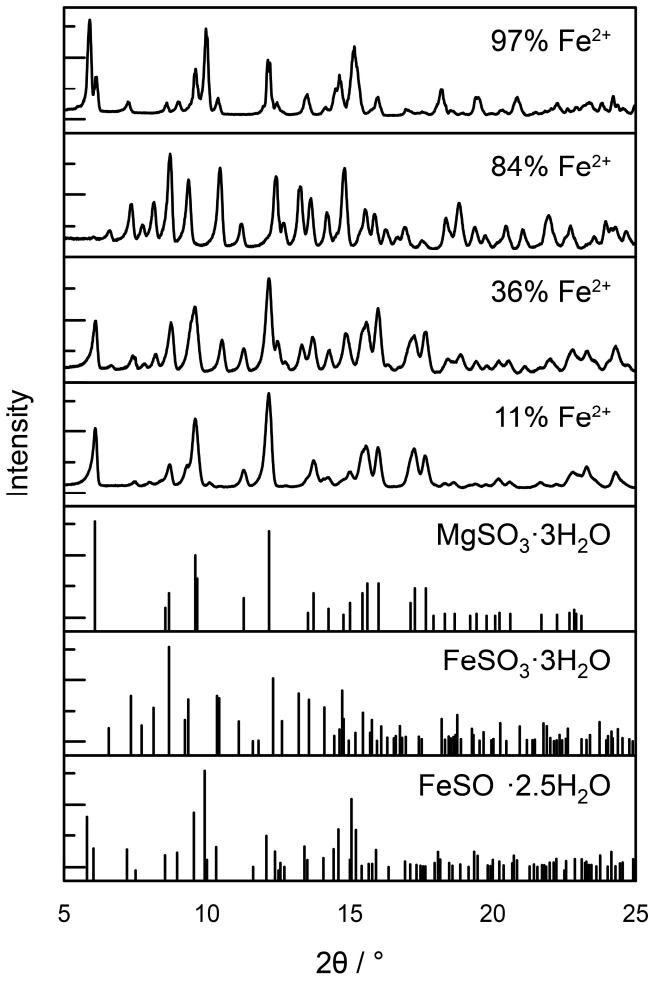

Fig. S12. X-ray diffraction patterns of sulfite solids with a range of Mg^{2+}/Fe^{2+} compositions. Measured PXRD for Mg^{2+}/Fe^{2+} sulfite solids with varying Fe^{2+} composition (11%, 36%, 84%, 97%) and reference patterns for $FeSO_3 \cdot 2.5H_2O$, $FeSO_3 \cdot 3H_2O$ and $MgSO_3 \cdot 3H_2O$. Performed with Mo X-ray source.

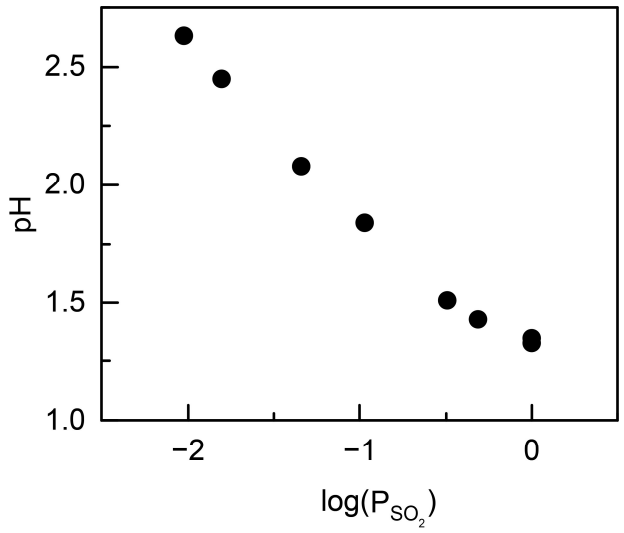

Fig. S13. Measured pH as a function of SO_2 pressure at room temperature in 1 M sodium bisulfite solution. Measured pH in a solution of 1M $NaHSO_3$ as a function of SO_2 pressure between 1 and 10^{-2} atm. The pressure of SO_2 was generated by flowing a mixture of SO_2 and N_2. The pH was recorded once the pH did not vary by more than 0.05 units for 5 minutes, and various pressures were measured in random order. Data collected at room temperature.

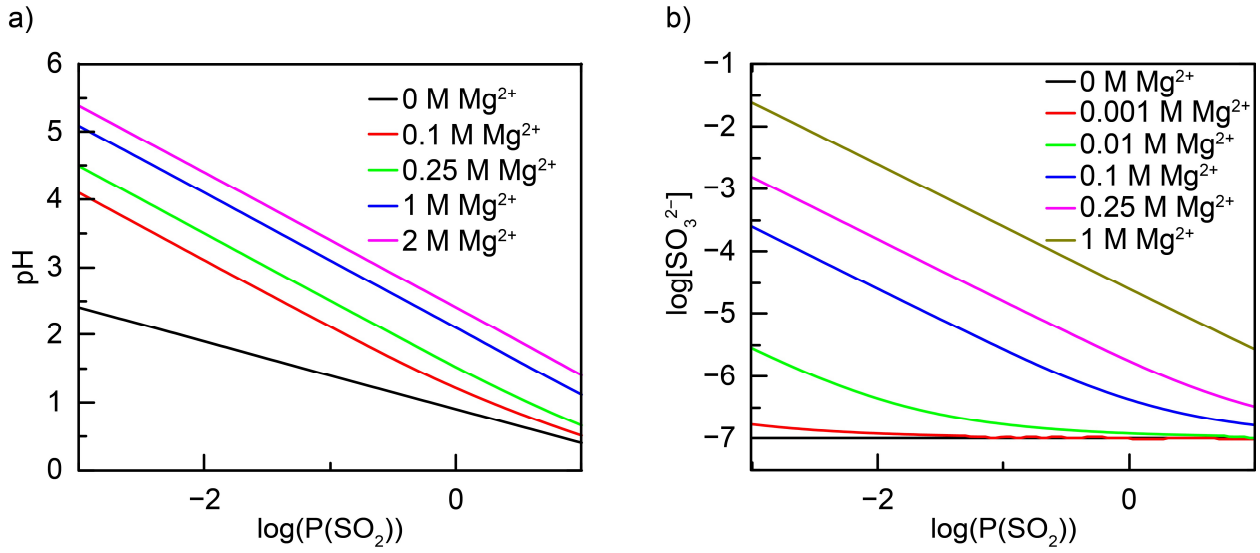

Fig. S14. Calculated thermodynamic relationships between pH, $[SO_3^{2-}]$, and SO_2 pressure in the absence of precipitating solids. a) Plots of calculated pH versus $\log(P_{SO2})$ for a variety of Mg^{2+} concentrations in the absence of solid precipitation. **b)** Plots of calculated $\log[SO_3^{2-}]$ versus $\log(P_{SO2})$ for a variety of Mg^{2+} concentrations in the absence of solid precipitation. Note that Mg^{2+} refers to MgO equivalents, as described in **Supplementary Note 2**

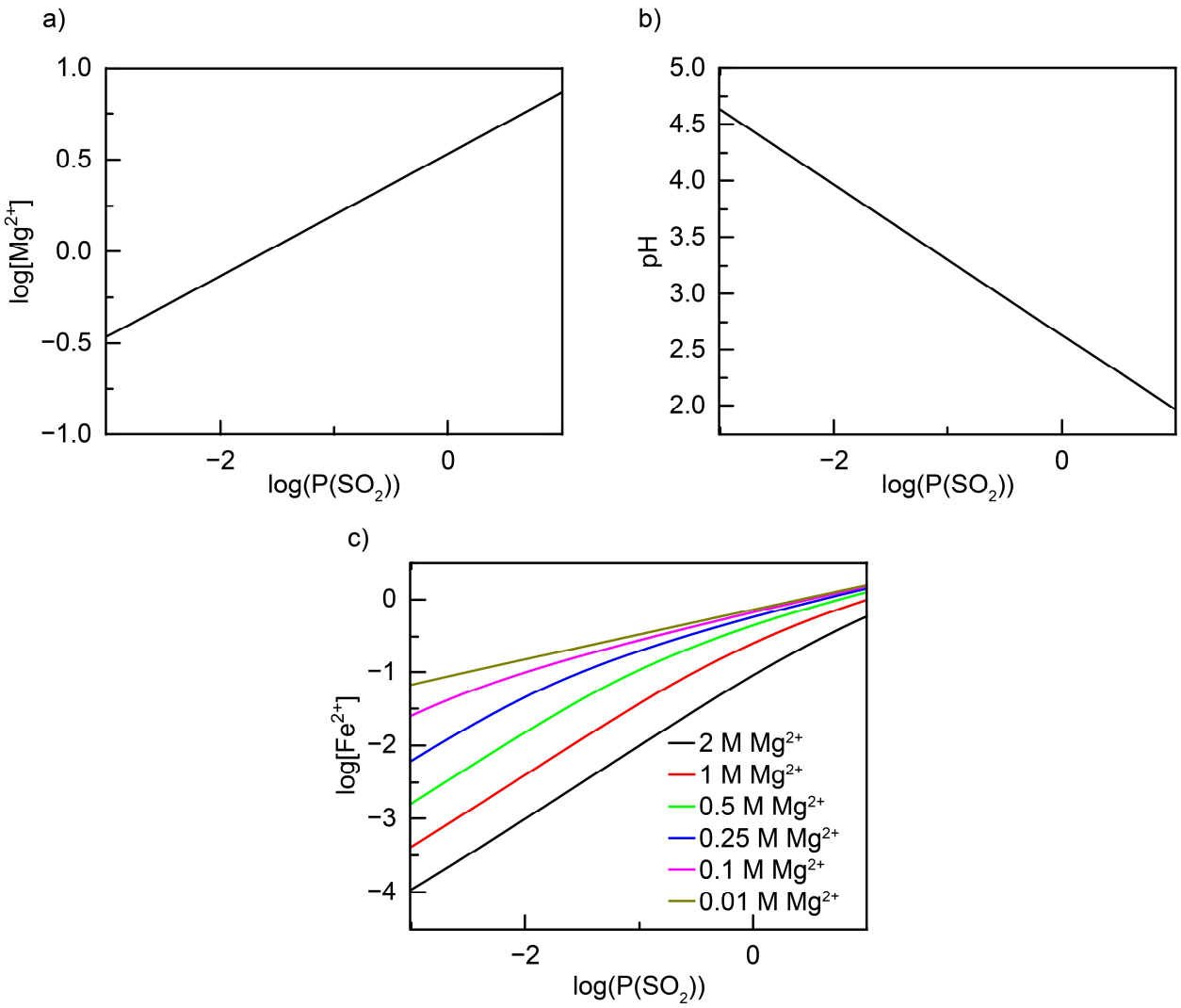

Fig. S15. Calculated thermodynamic relationships between pH, $[SO_3^{2-}]$, and SO_2 pressure in the presence of precipitating solids. a) Plots of calculated $\log[Mg^{2+}]$ versus $\log(P_{SO2})$ in the presence of $MgSO_3$ precipitation. **b)** Plots of calculated pH versus $\log(P_{SO2})$ in the presence of solid precipitation. **c)** Plots of calculated $\log[Fe^{2+}]$ versus $\log(P_{SO2})$ for a variety of Mg concentrations in the presence of $FeSO_3$ precipitation, but in the absence of $MgSO_3$ precipitation. Note that Mg^{2+} refers to MgO equivalents, as described in **Supplementary Note 2**

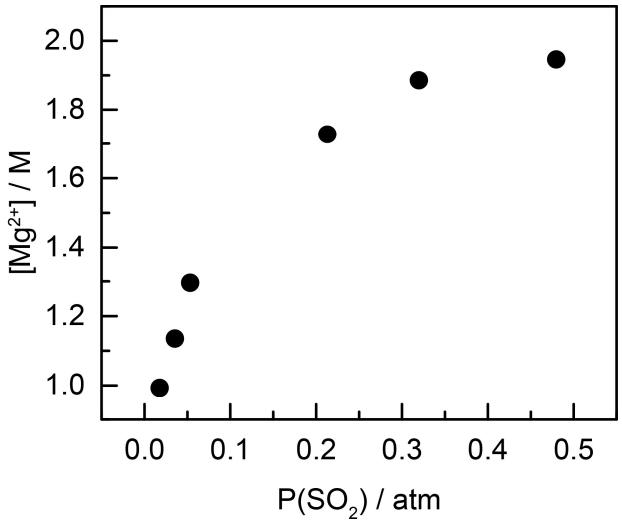

Fig. S16. Measured equilibrium $MgSO_3$ solubility as a function of SO_2 pressure. Measured equilibrium concentration of $[Mg^{2+}]$ in equilibrium with $MgSO_3 \cdot 3H_2O$ as a function of SO_2 pressure, 80 °C.

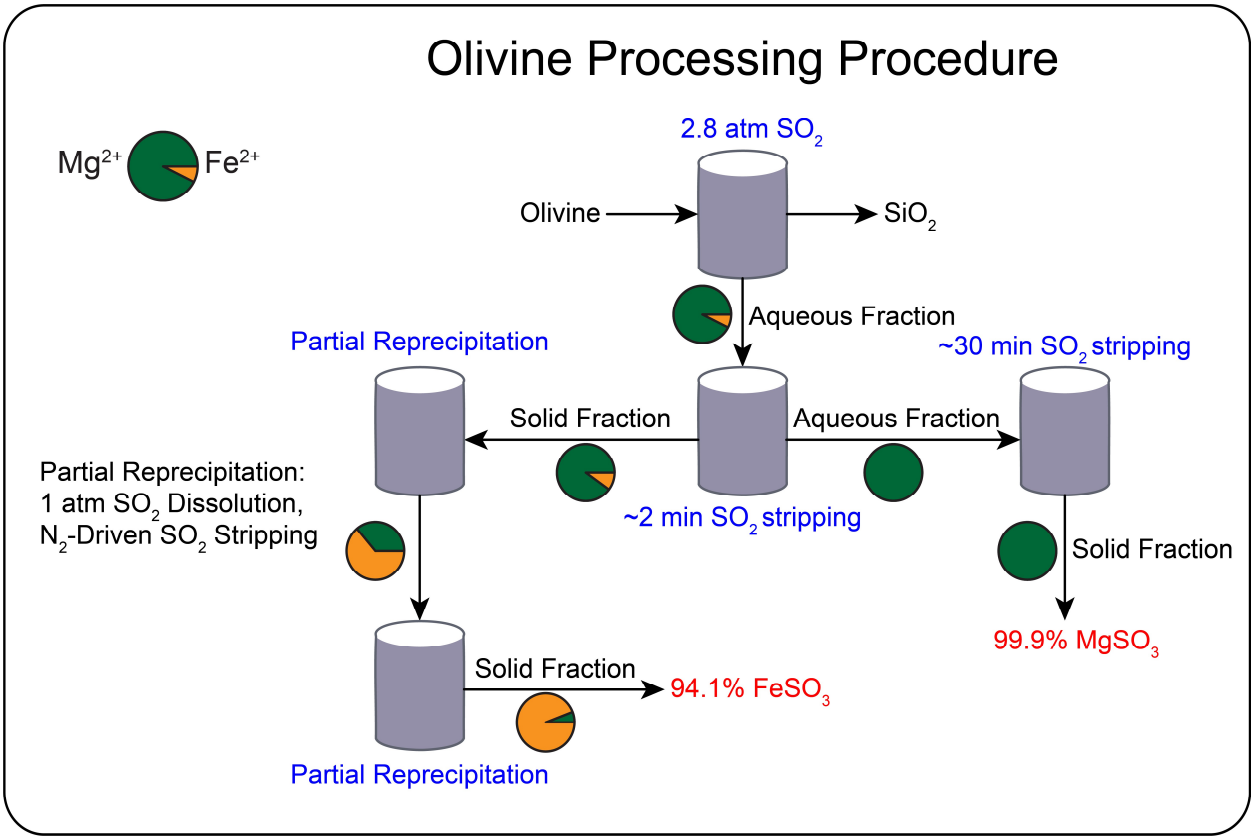

525 **Fig. S17. Schematic of olivine processing scheme for leaching and separating Mg^{2+} and Fe^{2+}.**
526 Schematic of olivine leaching and Mg^{2+}/Fe^{2+} separation through repeated SO_2 pressure swings, as described
527 in **Methods, Olivine Processing Tests – Leaching and Mg^{2+}/Fe^{2+} Separation**

528

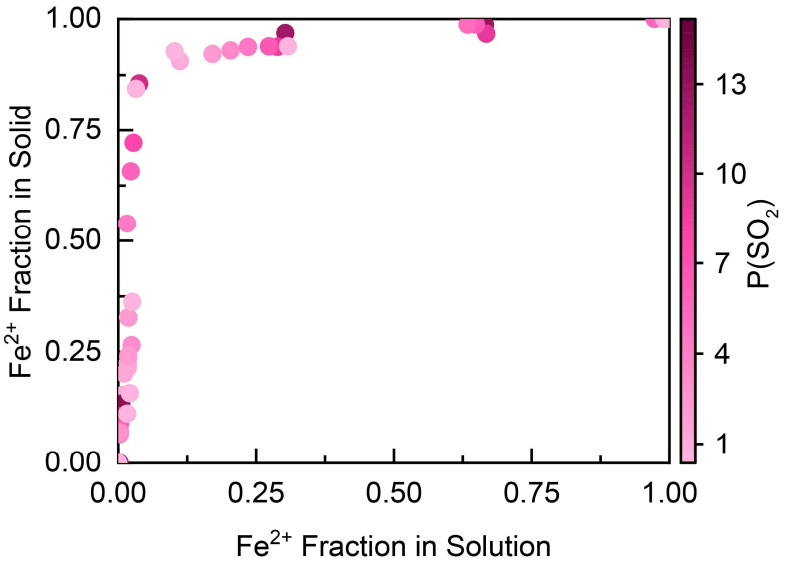

Fig. S18. Roozeboom plot with colormap indicating measured SO_2 pressure. Measured Fe^{2+} fraction in the precipitated phase as a function of measured Fe^{2+} fraction in solution for a range of pressures and Mg^{2+}/Fe^{2+} ratios between 0-100% Fe^{2+}, 80° C. Points are colored to represent SO_2 pressure with light pink representing low pressure and dark purple representing high pressures, as indicated by the color scale.

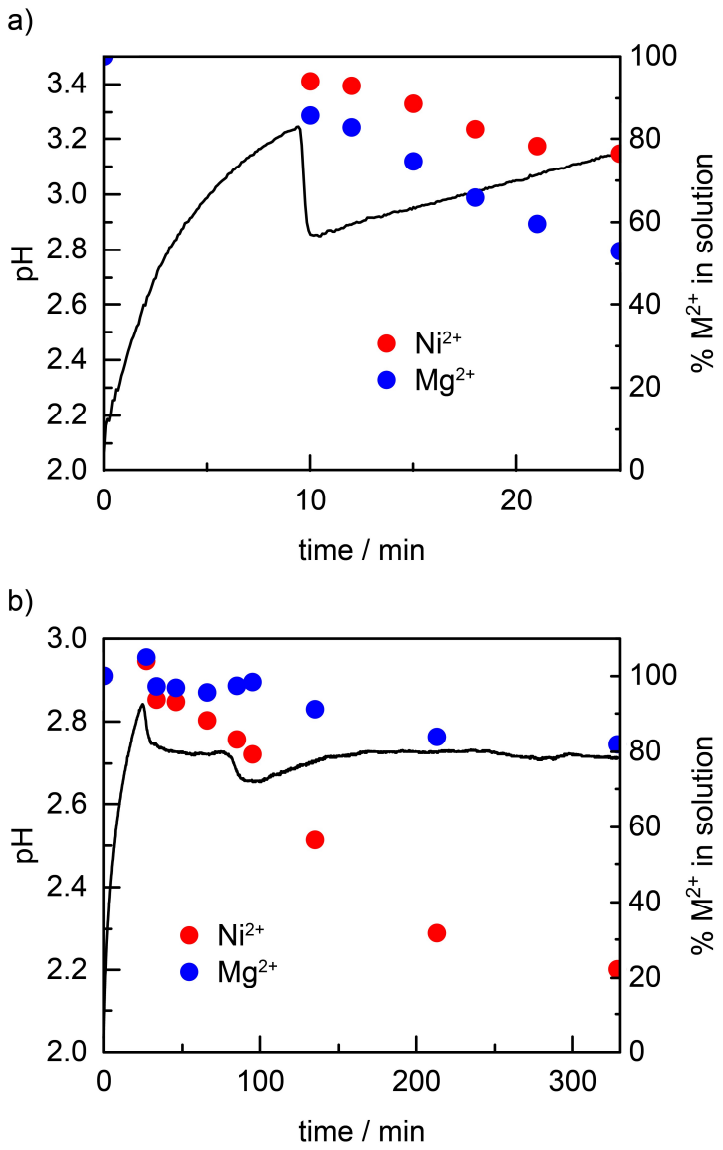

Fig. S19. Effect of SO_2 stripping rate during SO_2 stripping induced precipitation of Mg^{2+}/Ni^{2+} mixtures. a) Measured pH (black, left ordinate) and percent aqueous Mg^{2+} (blue, right ordinate) and Ni^{2+} (red, right ordinate) as a function of time while sparging a solution of $(Mg,Ni)(HSO_3)_2$ with 300 mL/min N_2. Concentrations of Mg and Ni are plotted relative to their concentration at t = 0, when there are no solids present. The Mg/Ni ratio is 98.9:1.1. Prior to time = 0, the solution is sparged with 1 atm SO_2 until complete dissolution of bisulfite precursors was observed. N_2 is introduced at time = 0. Experiment performed at 48° C. The peak in pH at 10 min corresponds to the first moment that solids are observed in solution. **b)** Measured pH (black, left ordinate) and percent aqueous Mg^{2+} (blue, right ordinate) and Ni^{2+} (red, right ordinate) as a function of time while sparging a solution of $(Mg,Ni)(HSO_3)_2$ solution with 20 mL/min N_2. Concentrations of Mg and Ni are plotted relative to their concentration at t = 0, when there are no solids present. The Mg/Ni ratio is 98.7:1.3. Prior to time = 0, the solution is sparged with 1 atm SO_2. N_2 is introduced at time = 0. Performed at 45° C. The peak in pH at 25 min corresponds to the first moment that solids are observed in solution.

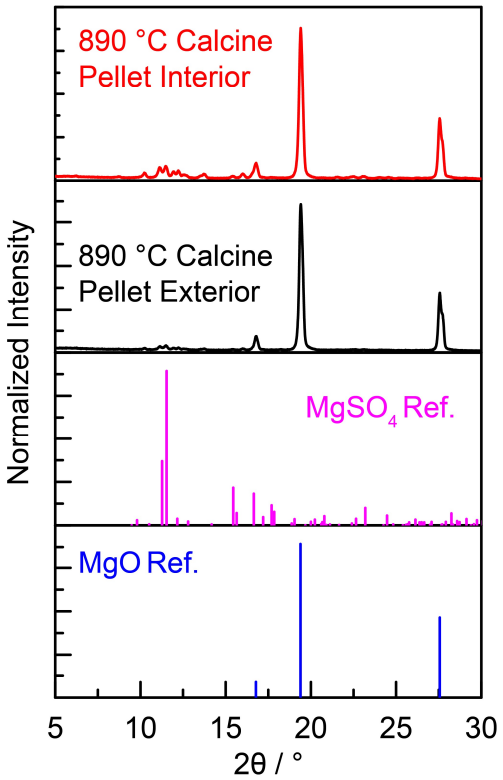

Fig. S20. X-ray diffraction patterns of $MgSO_3$ after calcination, comparing internal and external surface of the $MgSO_3$ pellet. Measured pXRD pattern of solid products after heating $MgSO_3 \cdot 3H_2O$ to 890 °C in an atmosphere of Ar. The $MgSO_3 \cdot 3H_2O$ was contained in a crucible with a pinhole to allow for gas exchange. After calcination, the solid product formed a pellet that was easily broken, from which samples were taken from the exterior surface (black) and interior (red) of the pellet for pXRD analysis. The reference patterns for MgO (blue) and $MgSO_4$ (magenta) are also shown. Performed with Mo X-ray source.

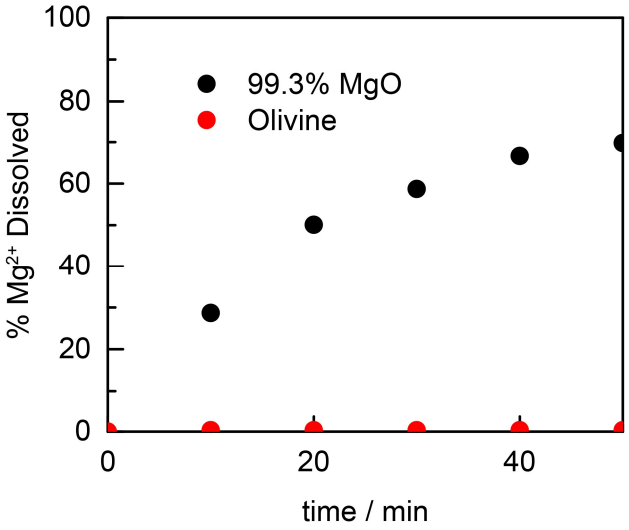

Fig. S21. Measured dissolution rate of olivine-derived MgO in 1 atm CO_2. Measured percent dissolution of Mg^{2+} from 99.3% MgO (red) generated from calcination of olivine-derived $MgSO_3$, and olivine (black) in 1 atm CO_2, r.t.

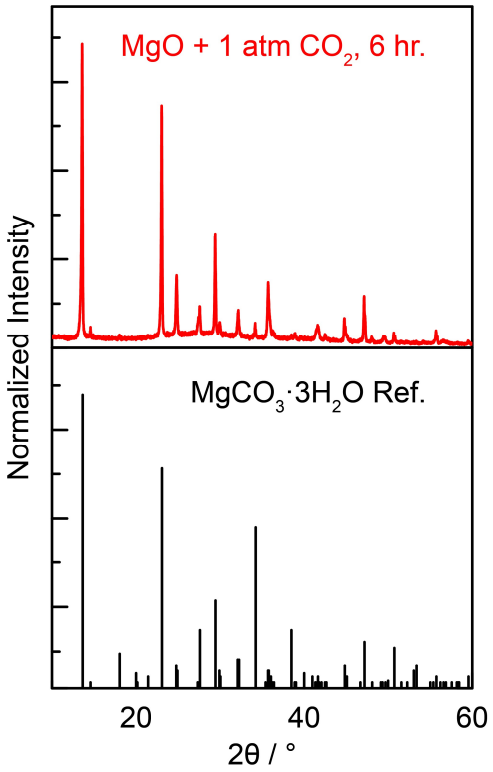

Fig. S22. X-ray diffraction pattern of $MgCO_3 \cdot 3H_2O$ formed from the reaction of olivine-derived MgO and CO_2 at room temperature. Measured pXRD pattern of solid products after exposing 99.3% MgO generated from processing olivine to 1 atm CO_2 in water for 6 hours (red) and reference pattern for $MgCO_3 \cdot 3H_2O$ (black). Performed with a Cu X-ray source.

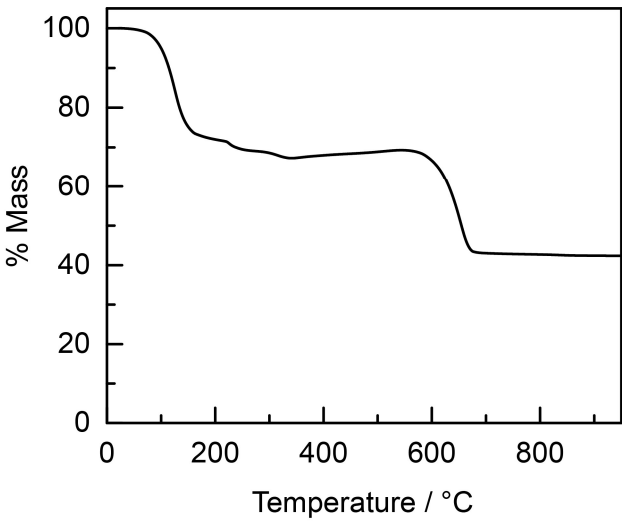

Fig. S23. Thermogravimetric analysis of $FeSO_3$•$3H_2O$ during calcination in air. Measured change in mass of $FeSO_3$•$3H_2O$ while heating in air at a ramp rate of 20 °C/min.

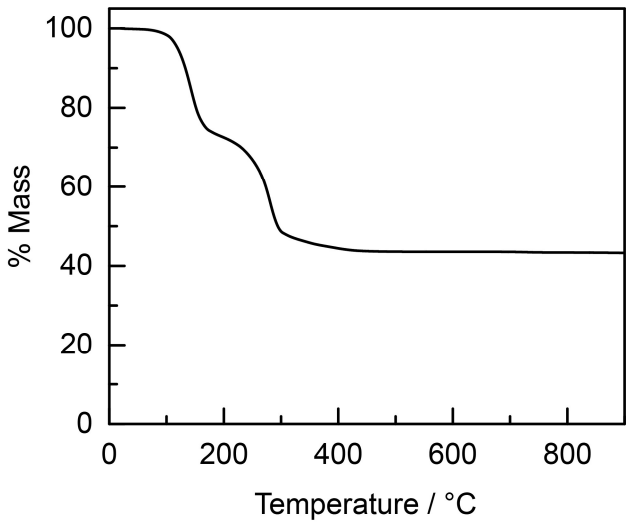

Fig. S24. Thermogravimetric analysis of $FeSO_3$•$3H_2O$ during calcination in N_2. Measured change in mass while heating $FeSO_3 \cdot 3H_2O$ in an N_2 atmosphere at a ramp rate of 20 °C/min.

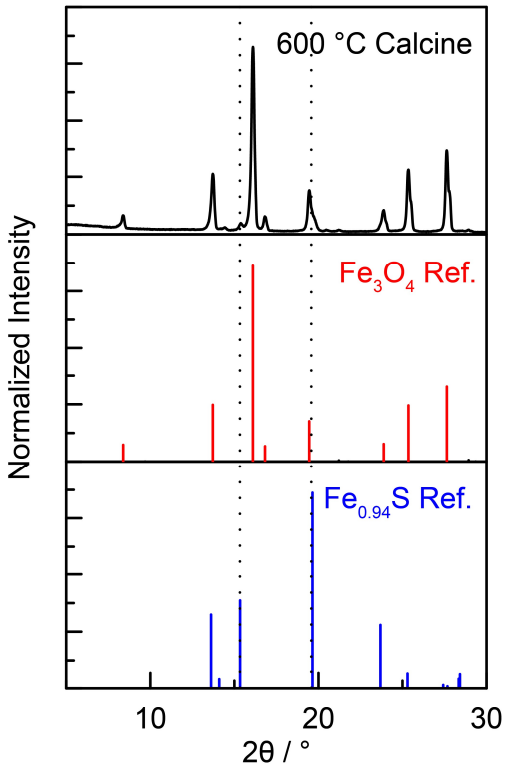

574 **Fig. S25. X-ray diffraction patterns of $FeSO_3 \cdot 3H_2O$ after calcination in N_2 600 °C.** pXRD pattern of
575 solid products after calcination of $FeSO_3 \cdot 3H_2O$ in an N_2 atmosphere at 600 °C for 1 hour (black) and
576 reference patterns for Fe_3O_4 (red) and $Fe_{0.94}S$ (blue). The dotted lines indicate the peaks assigned to the
577 $Fe_{0.94}S$ phase Performed with a Mo X-ray source.
578

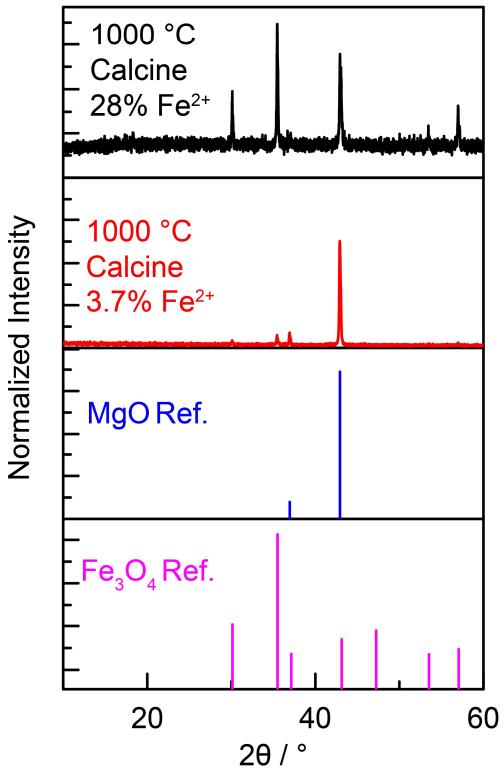

Fig. S26. X-ray diffraction patterns after calcination in N_2 at 1000 °C of $(Mg/Fe)SO_3 \cdot 3H_2O$ with varying Fe^{2+} concentration. pXRD pattern of solid products after calcination of $MgSO_3 \cdot 3H_2O$ in an N_2 atmosphere at 1000 °C for 20 min for $MgSO_3 \cdot 3H_2O$ containing 28% Fe^{2+} (black), $MgSO_3 \cdot 3H_2O$ containing 3.7% Fe^{2+}, and reference patterns for MgO (red) and Fe_3O_4 (magneta). Performed with a Cu X-ray source.

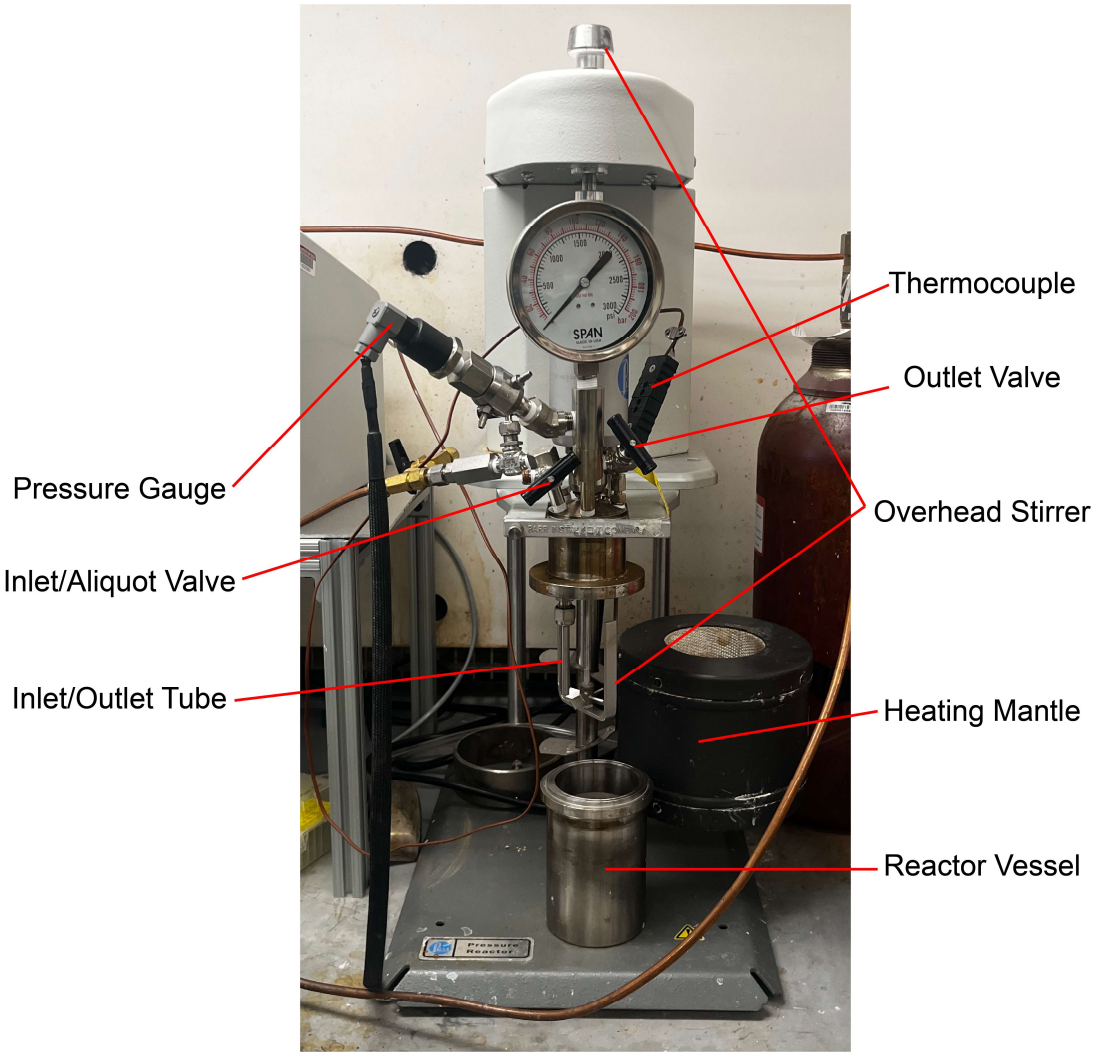

584 **Fig. S27. Schematic of experimental setup for leaching and precipitation experiments.** Optical
585 photograph of disassembled reactor used for olivine leaching and sulfite precipitation experiments.
586 Components of the reactor, as described in Methods, are labeled with red lines between the label and the
587 components location in the image.

588

Table S1. Standard Enthalpy of Formation Values. Compilation of standard enthalpy of formation values, $\Delta H_f°$, used for thermodynamic calculations.

Phase	$\Delta H_f°$, kJ/mol
$Mg_2SiO_{4(s)}$	−2174
$SO_{2(g)}$	−296
$H_2O_{(l)}$	−285
$H_2O_{(g)}$	−241
$Mg^{2+}_{(aq)}$	−466
$HSO_3^-{}_{(aq)}$	−626
$SiO_{2(am)}$	−903
$MgSO_3 \cdot 3H_2O_{(s)}$	−1932
$MgO_{(s)}$	−601
$NO_{2(g)}$	33
$O_{2(g)}$	0
$NO_3^-{}_{(aq)}$	−205
$Mg(NO_3)_2 \cdot 6H_2O_{(s)}$	−2613

References

1. Huss Jr., A. Studies of the catalysis and inhibition of the oxidation of aqueous sulfur(IV) solutions; effects on flue gas desulfurization processes. (University of Illinois at Urbana-Champaign, 1978).
2. Hall, S. 20 - Safety. in *Branan's Rules of Thumb for Chemical Engineers (Fifth Edition)* 321–336 (Butterworth-Heinemann, Oxford, 2012). doi:10.1016/B978-0-12-387785-7.00020-7.
3. Battino, R. Water. in *Oxygen and Ozone* vol. 7 1–40 (IUPAC-NIST, 1981).
4. Zhou, Q., Guo, H., Yang, P. & Wang, Z. Solubility of SO_2 in Water from 263.15 to 393.15 K and from 10 to 300 bar: Quantitative Raman Spectroscopic Measurements and PC-SAFT Prediction. *Ind. Eng. Chem. Res.* **59**, 12855–12861 (2020).
5. Rumpf, B. & Maurer, G. Solubilities of hydrogen cyanide and sulfur dioxide in water at temperatures from 293.15 to 413.15 K and pressures up to 2.5 MPa. *Fluid Phase Equilibria* **81**, 241–260 (1992).
6. Goldberg, R. N. & Parker, V. B. Thermodynamics of Solution of SO_2(g) in Water and of Aqueous Sulfur Dioxide Solutions. *J. Res. Natl. Bur. Stand.* **90**, 341–358 (1985).
7. Brantley, S. L., Kubicki, J. D. & White, A. F. Analysis of Rates of Geochemical Reactions. in *Kinetics of water-rock interaction* 1–38 (Springer Verlag, New York, 2008).
8. Ishihara, M., Matsui, H. & Hashizume, G. Thermal behaviour and S-O bonding state of alkaline-earth metal sulfites. *J. Therm. Anal. Calorim.* **38**, 1801–1815 (1992).
9. Saeki, Y., Matsuzaki, R., Kobayashi, T. & Masumizu, H. Thermal Decomposition Process of Magnesium Sulfite. *Gypsum Lime* **1979**, 59–65 (1979).
10. Schwitzegebel, Klaus. & Lowell, P. S. Thermodynamic basis for existing experimental data in magnesium-sulfur dioxide-oxygen and calcium-sulfur dioxide-oxygen systems. *Environ. Sci. Technol.* **7**, 1147–1151 (1973).
11. Scheidema, M. N. & Taskinen, P. Decomposition Thermodynamics of Magnesium Sulfate. *Ind. Eng. Chem. Res.* **50**, 9550–9556 (2011).
12. Scheidema, M. The reaction mechanism and operating window for the decomposition of hydrated magnesium sulfate under reducing conditions. (Aalto University, 2015).
13. Giauque, W. F. & Stephenson, C. C. Sulfur Dioxide. The Heat Capacity of Solid and Liquid. Vapor Pressure. Heat of Vaporization. The Entropy Values from Thermal and Molecular Data. *J. Am. Chem. Soc.* **60**, 1389–1394 (1938).
14. Streng, A. G. Miscibility and compatibility of some liquefied and solidified gases at low temperatures. *J. Chem. Eng. Data* **16**, 357–359 (1971).
15. Müller, H. Sulfur Dioxide. in *Ullmann's Encyclopedia of Industrial Chemistry* 73–118 (John Wiley & Sons, Ltd, 2000). doi:10.1002/14356007.a25_569.
16. Sporer, J. The Linde Solinox process: Gypsum-free flue-gas desulphurization. *Gas Sep. Purif.* **6**, 133–140 (1992).
17. Hudak, C. E. & Burke, J. M. *Summary Report: Sulfur Oxides Control Technology Series: Flue Gas Desulfurization, Wellman-Lord Process.* Report No. EPA 625/8-79-001 (Industrial Environmental Research Laboratory, 1979); https://nepis.epa.gov/Exe/ZyPDF.cgi/30004EB1.PDF?Dockey=30004EB1.PDF.
18. Wagman, D. D. *et al.* The NBS Tables of Chemical Thermodynamic Properties: Selected Values for Inorganic and C1 and C2 Organic Substances in SI Units. National Institute of Standards and Technology https://doi.org/10.18434/M32124 (2020).